A Family of High-Performance Cathode Materials for Na-ion Batteries, $Na_3(VO_{1-x}PO_4)_2F_{1+2x}$ $(0 \le x \le 1)$: Combined First-Principles and Experimental Study

*Young-Uk Park, Dong-Hwa Seo, Hyungsub Kim, Jongsoon Kim, Seongsu Lee, Byoungkook Kim, and Kisuk Kang**

Room-temperature Na-ion batteries (NIBs) have recently attracted attention as potential alternatives to current Li-ion batteries (LIBs). The natural abundance of sodium and the similarity between the electrochemical properties of NIBs and LIBs make NIBs well suited for applications requiring low cost and long-term reliability. Here, the first successful synthesis of a series of $Na_3(VO_{1-x}PO_4)_2F_{1+2x}$ $(0 \le x \le 1)$ compounds as a new family of high-performance cathode materials for NIBs is reported. The $Na_3(VO_{1-x}PO_4)_2F_{1+2x}$ series can function as high-performance cathodes for NIBs with high energy density and good cycle life, although the redox mechanism varies depending on the composition. The combined first-principles calculations and experimental analysis reveal the detailed structural and electrochemical mechanisms of the various compositions in solid solutions of $Na_3(VOPO_4)_2F$ and $Na_3V_2(PO_4)_2F_3$. The comparative data for the $Na_y(VO_{1-x}PO_4)_2F_{1+2x}$ electrodes show a clear relationship among $V^{3+}/V^{4+}/V^{5+}$ redox reactions, Na^+–Na^+ interactions, and Na^+ intercalation mechanisms in NIBs. The new family of high-energy cathode materials reported here is expected to spur the development of low-cost, high-performance NIBs.

1. Introduction

Sustainable energy production is an important advancement toward a sustainable society. The rapid depletion of fossil fuels and growing environmental concerns have stimulated the utilization of renewable energy sources, which is critical to a sustainable energy supply. However, challenges remain, including cost reduction and the efficient storage of energy. In particular, large-scale energy-storage systems (ESSs) are necessary for efficient utilization of renewable energies, such as solar and wind energy, whose production time does not correspond with consumption rates.[1–3] Li-ion batteries (LIBs), a candidate for ESSs, rely on limited and potentially expensive lithium resources; thus, LIBs may not be able to satisfy the demand for rapidly increasing renewable energy production.[1–3] On the other hand, room-temperature Na-ion batteries (NIBs) have recently been revisited as a possible alternative due to unlimited sodium resources from seawater.[1–8] Moreover, the close similarity between LIBs and NIBs has advanced the development of NIBs.

In the past few years, many oxides[9–13] and polyanion-based compounds[14–25] have been studied as NIB cathode materials. These materials primarily determine the performance of NIBs and account for a substantial part of the cost. Among cathode materials with promising electrochemical properties, recent studies have shown that sodium–vanadium fluorophosphates are outstanding due to their high energy densities (>500 Wh kg^{-1}) and the potential for multi-electron transfer of the vanadium redox couple.[26,27] The fluorophosphate framework provides a stable host with a low volumetric change during Na insertion/extraction.[26,28,29] These properties are particularly advantageous for NIBs, which typically undergo a large volumetric change with Na intercalation due to the larger ionic size of Na compared to Li, leading to poor cycle life. Additionally, while NIBs have exhibited a relatively low energy density due to the low potential of NIB cathodes, the inductive effects of both $(PO_4)^{3-}$ and F^- anions allow a high working potential in sodium–vanadium fluorophosphates.[26–30] Thus, the investigation of sodium–vanadium fluorophosphate chemistry

Y.-U. Park, Dr. D.-H. Seo, H. Kim, Dr. J. Kim, Prof. K. Kang
Department of Materials Science and Engineering
Seoul National University
1 Gwanak-ro, Gwanak-gu
Seoul 151-742, Republic of Korea
E-mail: matlgen1@snu.ac.kr

Dr. S. Lee
Korea Atomic Energy Research Institute
P.O. Box 105, Daejeon 305-600, Republic of Korea

Dr. B. Kim
Analysis Center for Research Advancement
Korea Advanced Institute of Science and Technology (KAIST)
291 Daehak-ro, Yuseong-gu
Daejeon 305-701, Republic of Korea

Prof. K. Kang
Center for Nanoparticle Research
Institute for Basic Science (IBS)
Seoul National University 1 Gwanak-ro
Gwanak-gu Seoul 151-742, Republic of Korea

Prof. K. Kang
Research Institute of Advanced Materials (RIAM)
Seoul National University
1 Gwanak-ro, Gwanak-gu, Seoul 151-742, Republic of Korea

DOI: 10.1002/adfm.201400561

is expected to advance the development of cathode materials that are well suited for NIBs.

To date, only a few sodium–vanadium fluorophosphates, including $Na_{1.5}VOPO_4F_{0.5}$,[15,31,32] $NaVPO_4F$,[16,17,33] $Na_3V_2(PO_4)_2F_3$,[18,19,34–37] and $Na_3V_2O_2(PO_4)_2F$,[20] have been independently reported as minerals or cathode materials for electrochemical systems. Around the same time, our group[26,28] and the Rojo group[27,30] first recognized that some of these compounds belong to the same crystallographic system of $Na_3(VO_{1-x}PO_4)_2F_{1+2x}$, where $x = 0$ corresponds to $Na_{1.5}VOPO_4F_{0.5}$ and $x = 1$ corresponds to $Na_3V_2(PO_4)_2F_3$. Although the Rojo group attempted to synthesize $Na_3(VO_{1-x}PO_4)_2F_{1+2x}$ ($0 \le x \le 1$),[27,29,30] and we recently succeeded in doping fluorine into $Na_{1.5}VOPO_4F_{0.5}$ ($x \approx 0.2$),[26,28] attempts to synthesize the solid solution often resulted in phases close to either $Na_3(VOPO_4)_2F$ ($x = 0$) or $Na_3V_2(PO_4)_2F_3$ ($x = 1$). Until now, the full solid solution of $Na_3(VO_{1-x}PO_4)_2F_{1+2x}$ could not be obtained. Herein, we report the successful synthesis of a family of $Na_3(VO_{1-x}PO_4)_2F_{1+2x}$ ($0 \le x \le 1$) and demonstrate their potential as new cathode materials for NIBs. We show that each compound of the $Na_3(VO_{1-x}PO_4)_2F_{1+2x}$ series can function as a high-performance cathode for NIBs with high energy density and good cycle life. Interestingly, the redox mechanism and phase reactions significantly varied depending on the composition, even though the compounds belong to the same crystal framework. We used a combined theoretical and experimental approach to determine the detailed reaction mechanisms of the $Na_3(VO_{1-x}PO_4)_2F_{1+2x}$ electrodes and show that their behavior varied with fluorine content. Finally, we propose a strategy for further increasing the energy density of the $Na_3(VO_{1-x}PO_4)_2F_{1+2x}$ electrodes by activating the multi-electron transfer of the vanadium redox couple.

2. Results and Discussion

2.1. Synthesis and Characterization of a Family of $Na_3(VO_{1-x}PO_4)_2F_{1+2x}$ ($0 \le x \le 1$) Compounds

Substantial changes in the anion composition in a crystal generally result in the formation of impurities or second phases because the anions are usually the main building blocks of crystals. Moreover, substitution with aliovalent anions accompanies a simultaneous change in the oxidation states of the cations, which often complicates the synthesis of pure phases. Nevertheless, we found that a series of $Na_3(VO_{1-x}PO_4)_2F_{1+2x}$ compounds can be obtained in the same crystal framework with a full range of $0 \le x \le 1$. The similar synchrotron X-ray diffraction (XRD) patterns of $Na_3(VO_{1-x}PO_4)_2F_{1+2x}$ powders (x = 0.0, 0.2, 0.5, 0.8, and 1.0) indicate that they belong to an isostructural system (**Figure 1**a). The continuous peak shift with varying composition of $Na_3(VO_{1-x}PO_4)_2F_{1+2x}$ ($0 \le x \le 1$) also implies a complete solid solution over this composition range (Figure 1a, insets). We also confirmed that the fluorine content in $Na_3(VO_{1-x}PO_4)_2F_{1+2x}$ changed linearly with the targeted composition (x) from the energy-dispersive X-ray spectroscopy (EDS) and inductively coupled plasma (ICP) analyses (see Supporting Information, Figure S1). The particle sizes and morphologies of the $Na_3(VO_{1-x}PO_4)_2F_{1+2x}$ powders (x = 0.0, 0.2, 0.5, 0.8, and 1.0) were examined by scanning electron microscopy (SEM) and transmission electron microscopy (TEM). The SEM images showed particle sizes in the range of 1–5 μm (see Supporting Information, Figure S2), and the TEM images and corresponding selected-area electron diffraction (SAED) data suggested that most of the micron-sized particles were single-crystalline with the same tetragonal symmetry (Figure 1b–e).

To closely monitor the crystal structure of isostructural $Na_3(VO_{1-x}PO_4)_2F_{1+2x}$ ($0 \le x \le 1$) compounds, we carried out neutron diffraction (ND) and XRD analyses for the samples (x = 0.0, 0.2, 0.5, 0.8, and 1.0). Based on the combined ND and XRD refinements of each sample, the lattice parameters continuously changed with increasing fluorine content in $Na_3(VO_{1-x}PO_4)_2F_{1+2x}$ ($0 \le x \le 1$) (see **Table 1** and Supporting Information Figure S3–S4, Table S1–S15 for the detailed results of the combined ND and XRD refinements). **Figure 2**a–d show that lattice parameter a increased slightly, whereas lattice parameter c and volume V increased significantly with increasing fluorine content. The continuous lattice change confirmed the formation of the solid solution. The asymmetric lattice variations with the fluorine content (a vs. c) can be understood as follows. Lattice parameter c results from the sum of the height (h) of V^{n+} octahedra and the distance (d) between terminal anions, as shown in Figure 2e. When x increases from 0 to 1, h increases due to the larger V^{3+} octahedra relative to V^{4+}. On the other hand, d decreases due to the increase in fluorine content, which exhibits weaker F^-–F^- repulsion compared to O^{2-}–O^{2-} repulsion (see Supporting Information Figure S5 for the variation of h and d with increasing x). However, the increase in h is much more pronounced than the reduction of d, because the expansion of vanadium octahedra from V^{4+} to V^{3+} leads to a greater elongation along the c-axis (the direction of h) than the a- or b-axis. This anisotropic change is attributable to the distorted characteristics of V^{4+} octahedra. As Whittingham et al. noted,[38] V^{4+} ions usually form a distorted octahedron due to the exceptionally short vanadyl bond, unlike V^{3+} ions, which are prone to form a regular octahedron. In our samples, the refinement results in **Table 2** showed a very short vanadyl V1–O4 bond (~1.63 Å) along the c-axis for $V^{4+}O_5F$ octahedra (x = 0; Figure 2f) compared to V–O(F) bonds (~2.0 Å) for $V^{3+}O_4F_2$ octahedra (x = 1; Figure 2g). Baur's distortion indices[39] (Δ) in Table 2 also confirm that the $V^{4+}O_5F$ octahedra were much more distorted than the $V^{3+}O_4F_2$ octahedra. As x increased, changes in the octahedral volume were accommodated by the recovery of the V–O(F) bond length from the short vanadyl bond along the c-axis, leaving the lattice parameter a nearly constant.

The variation in the fluorine content of $Na_3(VO_{1-x}PO_4)_2F_{1+2x}$ ($0 \le x \le 1$) shifted the oxidation state of vanadium, which eventually affected the electrochemical reaction mechanism. According to X-ray absorption near-edge structure (XANES) analysis of the vanadium K-edge (Figure 2h), the vanadium oxidation state continuously changed with fluorine content (x). As x increased from 0 to 1, the edge of the spectrum shifted toward lower energy, indicating the reduction of the vanadium ion. A clearer change was observed in the pre-edge region (Figure 2h, inset), where the pre-edge peak gradually became smaller with increasing x and finally disappeared at $x = 1$. This

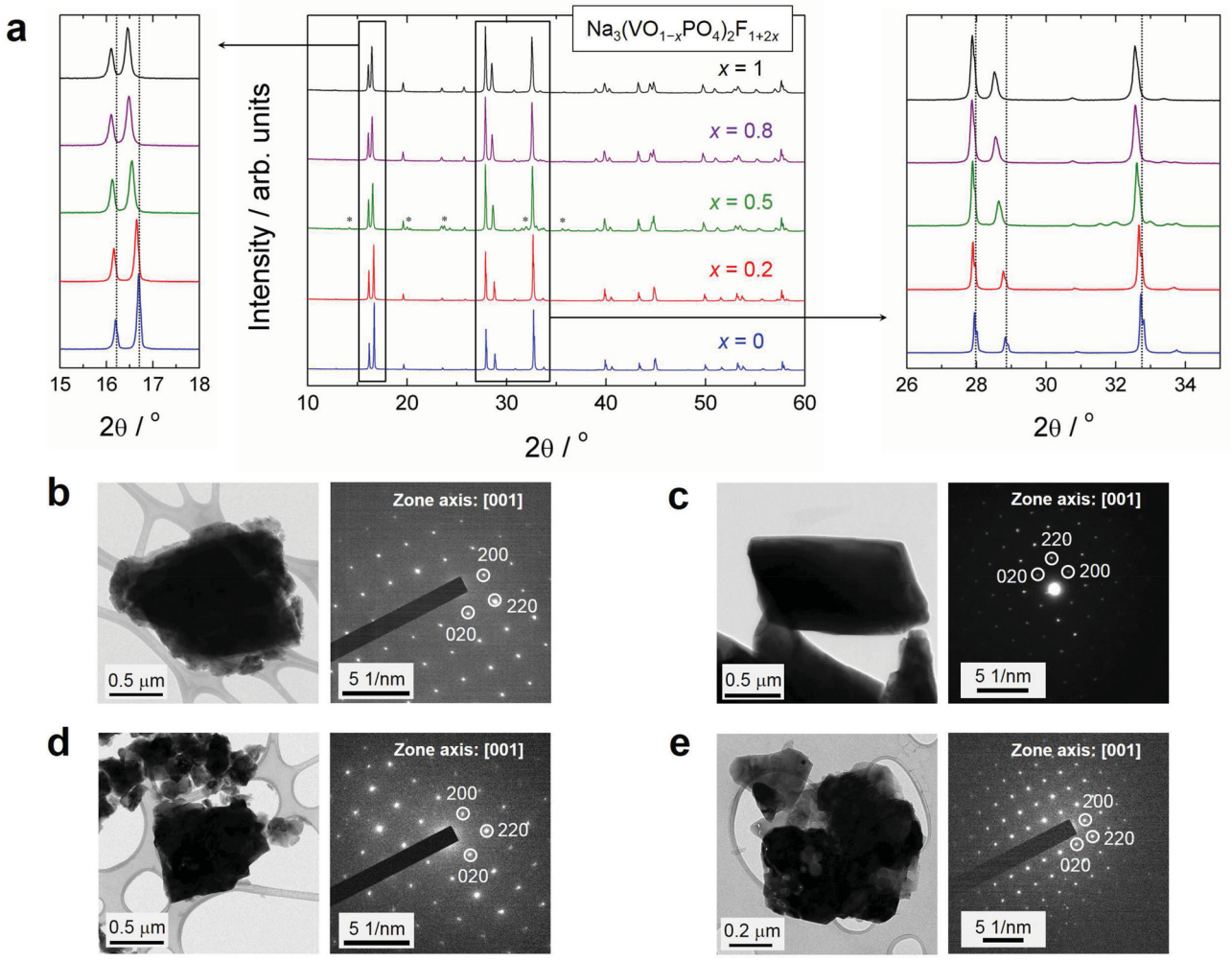

Figure 1. (a) XRD patterns of the $Na_3(VO_{1-x}PO_4)_2F_{1+2x}$ (x = 0.0, 0.2, 0.5, 0.8, and 1.0) powders. Reflections denoted by asterisks are from the rhombohedral $Na_3V_2(PO_4)_3$, which is an impurity in x = 0.5. (b–e) Bright-field TEM images (left) and the corresponding SAED patterns (right); (b) x = 0.0, (c) x = 0.2, (d) x = 0.8, and (e) x = 1.0.

observation agrees with previous XANES work for compounds containing V^{4+} and V^{3+} ions.[40,41] Compounds with distorted V^{4+} octahedra generally exhibit a large pre-edge peak, whereas those with V^{3+} octahedra show a negligible pre-edge peak due to the much weaker $1s \rightarrow 3d$ transition.[38,41] The gradual disappearance of the pre-edge peak with increasing x agrees with the

Table 1. Lattice parameters of the $Na_3(VO_{1-x}PO_4)_2F_{1+2x}$ samples (x = 0.0, 0.2, 0.5, 0.8, and 1.0) from the combined ND and XRD refinement (Space group: $P4_2/mnm$).

x	ND or XRD	a [Å]	c [Å]	V [Å^3]
0.0	ND	9.02257(13)	10.61358(18)	864.02(2)
	XRD[a)]	9.02726(1)	10.61877(3)	865.340(3)
0.2	ND	9.03330(11)	10.63004(16)	867.42(2)
	XRD[a)]	9.03404(4)	10.63059(6)	867.603(7)
0.5	ND	9.0326(2)	10.6917(3)	872.32(4)
	XRD[a)]	9.03433(6)	10.69451(7)	872.877(9)
0.8	ND	9.0341(2)	10.7299(4)	875.73(4)
	XRD[a)]	9.03725(9)	10.73107(12)	876.427(16)
1.0	ND	9.03635(9)	10.74843(14)	877.670(17)
	XRD[a)]	9.0350(2)	10.7408(3)	876.79(4)

[a)]synchrotron X-ray source

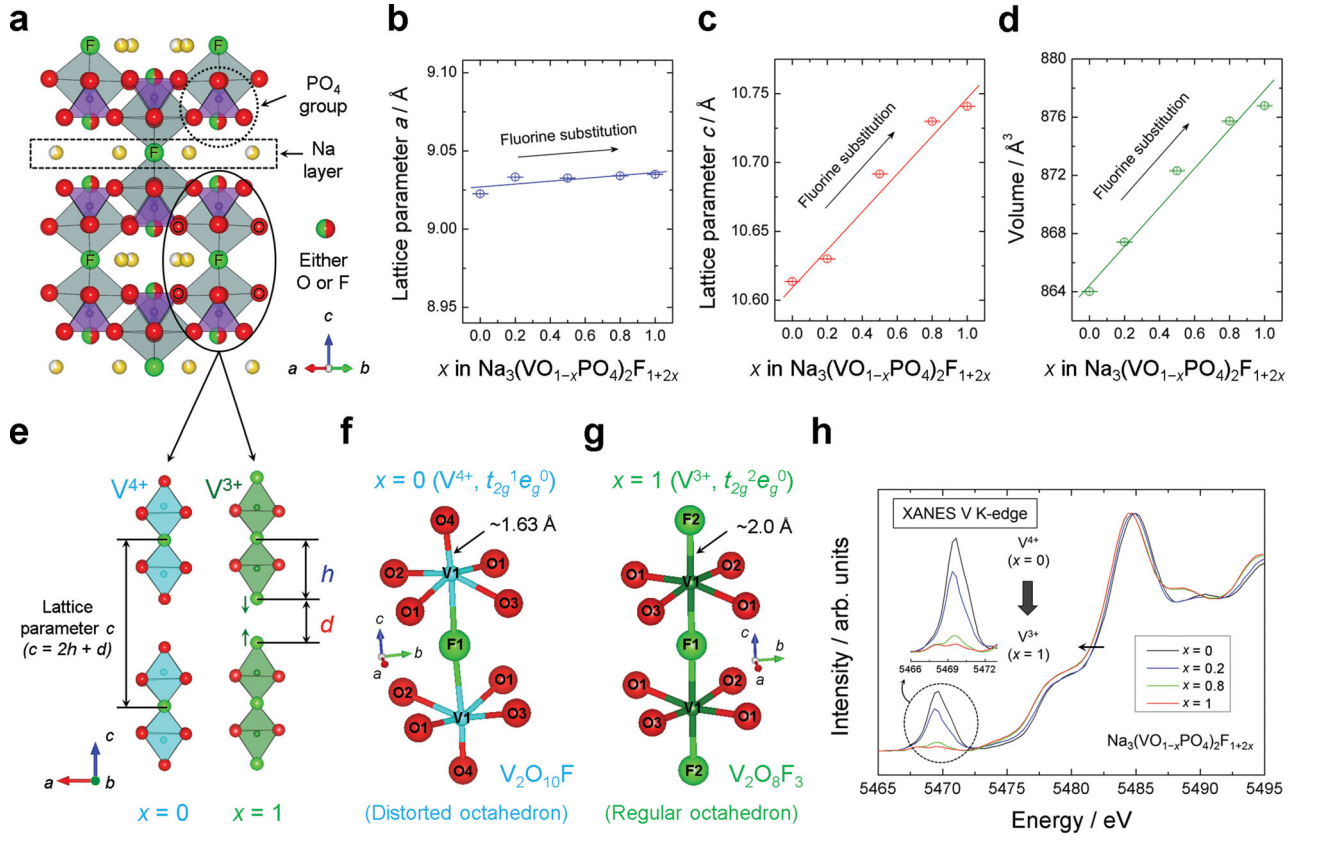

Figure 2. (a) Crystal structure of $Na_3(VO_{1-x}PO_4)_2F_{1+2x}$ ($0 \le x \le 1$). Oxygen and fluorine ions are shown as red and green spheres, respectively. (b–d) Lattice parameter change of $Na_3(VO_{1-x}PO_4)_2F_{1+2x}$ ($0 \le x \le 1$) based on the ND data; (b) lattice parameter *a*, (c) lattice parameter *c*, (d) unit cell volume. (e) Components of lattice parameter *c*. (f) Geometry of the $V_2O_{10}F$ bioctahedron for $x = 0$ (V^{4+}, $t_{2g}{}^1e_g{}^0$). (g) Geometry of the $V_2O_8F_3$ bioctahedron for $x = 1$ (V^{3+}, $t_{2g}{}^2e_g{}^0$). (h) Vanadium K-edge XANES spectra of the $Na_3(VO_{1-x}PO_4)_2F_{1+2x}$ samples with different fluorine contents; $x = 0.0$ (black), $x = 0.2$ (blue), $x = 0.8$ (green), and $x = 1.0$ (red). The inset shows an enlarged graph of the pre-edge region.

structural analysis, which showed that $V^{4+}O_5F$ octahedra were much more distorted than $V^{3+}O_4F_2$ octahedra.

Further atomic analysis of series of $Na_3(VO_{1-x}PO_4)_2F_{1+2x}$ ($0 \le x \le 1$) was performed using ^{23}Na magic-angle spinning (MAS) nuclear magnetic resonance (NMR) (see Supporting Information for the detailed explanation). **Figure 3** shows ^{23}Na MAS NMR spectra of $Na_3(VO_{1-x}PO_4)_2F_{1+2x}$ (x = 0.0, 0.2, 0.5, 0.8, and 1.0). According to the modified Goodenough–Kanamori rules,[42,43] unpaired electron spins of V^{4+} ions ($t_{2g}{}^1e_g{}^0$) or V^{3+} ions ($t_{2g}{}^2e_g{}^0$) are transferred to Na 3*s* orbitals via O 2*p* (or F 2*p*) orbitals; thus, large and positive Fermi-contact shifts are expected in ^{23}Na MAS NMR spectra, as illustrated in Figure 3a.

Table 2. Bond distances of V–O(F) bonds, Baur's distortion indices (Δ), and octahedral volumes of VO_5F ($x = 0$) and VO_4F_2 ($x = 1$) octahedra from the refinement results (see Supporting Information, Table S1–S3 and S13–S15).

x	Type of bioctahedron (or octahedron)	Electronic configuration of V^{n+} ions	V–O(F) bonds	Bond distance [Å]	Baur's distortion index (Δ)	Octahedral volume [Å^3]
0	$V_2O_{10}F(VO_5F)$	V^{4+} ($t_{2g}{}^1e_g{}^0$)	V1–O1 (×2)	1.988(6)	0.05592	9.6670
			V1–O2 (×1)	1.992(6)		
			V1–O3 (×1)	2.053(6)		
			V1–F1 (×1)	2.11682(5)		
			V1–O4 (×1)	1.6327(16)		
1	$V_2O_8F_3(VO_4F_2)$	V^{3+}($t_{2g}{}^2e_g{}^0$)	V1–O1 (×2)	1.966(9)	0.01482	10.2295
			V1–O2 (×1)	1.957(8)		
			V1–O3 (×1)	2.061(8)		
			V1–F1 (×1)	1.991(3)		
			V1–F2 (×1)	1.953(4)		

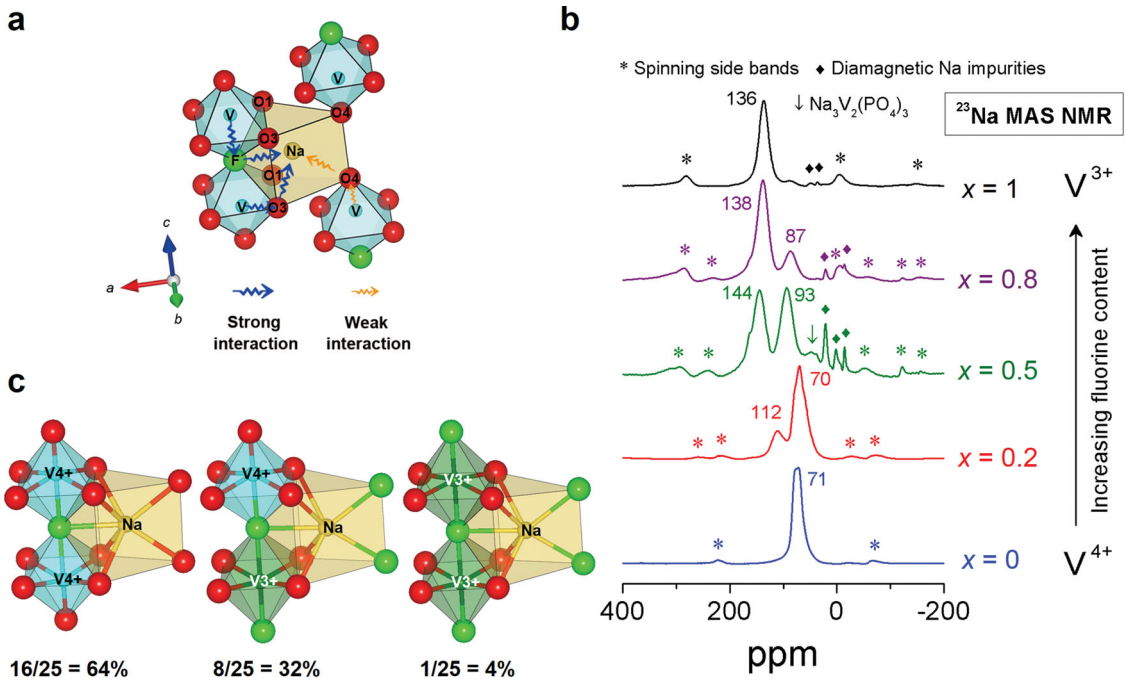

Figure 3. (a) Schematic representation of various types of Na–O(F)–V interactions in the crystal structure of $Na_3(VOPO_4)_2F$ ($x = 0$). Strong and weak interactions are denoted by blue and orange arrows, respectively. (b) ^{23}Na MAS NMR spectra of the $Na_3(VO_{1-x}PO_4)_2F_{1+2x}$ samples with different fluorine contents ($x = 0.0$, 0.2, 0.5, 0.8, and 1.0) at a MAS spinning speed of 15 kHz; spinning side bands are marked with asterisks. Diamagnetic Na impurities are denoted by diamonds. A broad peak at ~45 ppm for $x = 0.5$ (denoted by an arrow) may originate from an impurity phase of $Na_3V_2(PO_4)_3$. (c) Three types of possible local environments for vanadium bioctahedra for $x = 0.2$ and their expected abundance ratio when the ratio of V^{4+} to V^{3+} ions is 4:1.

Na ions can receive unpaired electron spins from four adjacent vanadium ions via seven neighboring anions (O1, O3, O4, or F1 2*p* orbitals for Na1 site), and most angles for the Na–O(F)–V interactions were around 90° (see Supporting Information, Table S16). This type of interaction can transfer a large amount of electron spin density (strong interactions; denoted by blue arrows), whereas an interaction deviating from 90°, such as the Na1–O4–V1 interaction, can transfer only a small amount of the electron spin density of V^{4+} ions (weak interactions; denoted by orange arrows). Consequently, most of the transferred electron density of a Na atom was not from corner-sharing VO_5F octahedra but from face-sharing $V_2O_{10}F$ bioctahedra. This enabled a partial view of the distribution of V^{3+} and V^{4+} ions in the structure. The ^{23}Na MAS NMR spectra in Figure 3b show single, strong Fermi-contact shifts (71 and 136 ppm) for two end members of $Na_3(VOPO_4)_2F$ ($x = 0$) and $Na_3V_2(PO_4)_2F_3$ ($x = 1$), respectively, indicating a single valence state for the vanadium ions. The gap between the two Fermi-contact shifts was *ca.* 65 ppm, mainly due to the difference in the number of unpaired electrons in V^{4+} (d^1) and V^{3+} (d^2) ions. This difference is similar to the gap between ^7Li NMR shifts of $LiV^{3+}PO_4F$ and $Li_2V^{2+}PO_4F$, which is known to be 60–70 ppm.[44] For intermediate fluorine contents ($x = 0.2$, 0.5, and 0.8), more than two isotropic resonances were observed. In the case of $Na_3(V^{3.8+}O_{0.8}PO_4)_2F_{1.4}$ ($x = 0.2$), two major Fermi-contact shifts were detected at 70 and 112 ppm, indicating that two types of paramagnetic sources having a different number of unpaired electrons coexisted in the crystal. V^{3+} ions cause a larger positive Fermi-contact shift due to the greater paramagnetic nature relative to V^{4+} ions; thus, the two peaks centered at 70 and 112 ppm are attributable to Na neighboring V^{4+} and V^{3+} ions, respectively.

The mixed valences of V^{3+} and V^{4+} led to three types of local environments for strong 90° interactions between Na and vanadium bioctahedra in the intermediate compositions of $Na_3(VO_{1-x}PO_4)_2F_{1+2x}$ ($x = 0.2$, 0.5, and 0.8), as shown in Figure 3c. Assuming that the V^{4+} and V^{3+} ions are homogeneously mixed in the crystal with a ratio of 4:1 for $Na_3(V^{3.8+}O_{0.8}PO_4)_2F_{1.4}$ ($x = 0.2$),[28] the abundance ratios are expected to be 64, 32, and 4% for the three environments. The observed intensity ratio of about 3:1 for the peaks at 70 and 112 ppm suggests that the Fermi-contact shift at 70 ppm is most likely due to the interaction between Na and $(V^{4+})_2O_{10}F$ bioctahedra. Interestingly, the peak related to V^{3+} ions had a considerably less positive NMR shift ($x = 0.2$; 112 ppm) compared to that of $Na_3V_2(PO_4)_2F_3$ ($x = 1$; 136 ppm). This suggests that most of the Na atoms affected by V^{3+} ions (d^2) had at least one weak interaction with V^{4+} ions (d^1) and implies that V^{4+} and V^{3+} ions were rather randomly mixed at the atomic level in the crystal. A similar explanation is also valid for $Na_3(V^{3.2+}O_{0.2}PO_4)_2F_{2.6}$ ($x = 0.8$) having two Fermi-contact shifts at 138 ppm (related to V^{3+} ions) and 87 ppm (related to V^{4+} ions) with an intensity ratio of 3:1. The peak related to V^{4+} ions had a considerably more positive NMR shift ($x = 0.8$; 87 ppm) compared to that of $Na_3(VOPO_4)_2F$ ($x = 0$; 71 ppm), also implying similar distribution of V^{4+} and V^{3+} ions at the atomic level. More discussion on the NMR results can be found in the Supporting Information including Table S16.

2.2. Electrochemical Reaction Mechanisms of the $Na_y(VO_{1-x}PO_4)_2F_{1+2x}$ ($0 \le x \le 1$) Electrodes

Figure 4a and b show the voltage–composition curves of the $Na_y(VO_{1-x}PO_4)_2F_{1+2x}$ (x = 0.0, 0.2, 0.5, 0.8, and 1.0) electrodes. It is noteworthy that all the $Na_y(VO_{1-x}PO_4)_2F_{1+2x}$ electrodes showed the similar average voltage of 3.8–3.9 V (vs. Na^+/Na) and the capacity of 120–130 mAh g^{-1}. Also, all the $Na_y(VO_{1-x}PO_4)_2F_{1+2x}$ electrodes exhibited roughly similar voltage–composition profiles regardless of fluorine content. The notably smaller charge capacity and larger irreversible capacity of the first cycle for x = 0.5 may be due to impurity phases in the sample. However, while electrodes with lower x values (x = 0.0, 0.2, and 0.5) in Figure 4a showed two voltage plateaus with a step at $y \approx 2.0$, those with higher x values (x = 0.8 and 1.0) in Figure 4b exhibited four voltage plateaus; the two additional steps at $y \approx 2.43$ and 1.55 are shown more closely in the inset of Figure 4b. The presence of the voltage steps suggests multiple phase transitions due to Na contents in $Na_y(VO_{1-x}PO_4)_2F_{1+2x}$, and the difference in electrochemical steps implies the sensitive influence of fluorine content on the phase reaction. Notably, similar average voltages were observed despite the different redox couples of V^{3+}/V^{4+} and V^{4+}/V^{5+}. While the end members of $Na_3(VO_{1-x}PO_4)_2F_{1+2x}$ had either only the V^{4+}/V^{5+} redox couple for x = 0 or only the V^{3+}/V^{4+} redox couple for x = 1, the V^{4+}/V^{5+} redox potential of the former (~3.77 V vs. Na^+/Na) was lower than the V^{3+}/V^{4+} redox potential of the latter (~3.9 V vs. Na^+/Na) by ~0.13 V, as shown in Figure 4c. This indicates that the strong inductive effect of fluorine ions in fluorine-rich samples could raise the V^{3+}/V^{4+} redox potential substantially. Typically, the redox potential of V^{3+}/V^{4+} is lower than that of V^{4+}/V^{5+} by ~0.66 V under standard conditions.[45] However, this difference could be counterbalanced by the voltage gain from the stronger inductive effect. Furthermore, this cancellation resulted in a net voltage gain of +0.13 V. Figure 4c shows that the average voltage changed linearly over the full range of fluorine contents ($0 \le x \le 1$).

All the samples showed distinct voltage steps at $y \approx 2.0$ in the electrochemical profile, indicating the presence of a stable intermediate phase for this composition. The phase stabilization at $y \approx 2.0$ is believed to originate from the significantly relieved Na^+–Na^+ repulsion at this particular Na composition, as schematically shown in Figure 4d. The reduction in Na^+–Na^+ repulsion at $y \approx 2.0$ occurs *via* (i) Na extraction [n = 3 → 2; blue arrows] and (ii) Na-vacancy re-ordering [n = 2 (*cis*) → 2 (*trans*); red arrows]. The unique diagonal Na configuration (*i.e.*, *trans* configuration), minimizing the electrostatic repulsion, is possible at this composition and is believed to stabilize

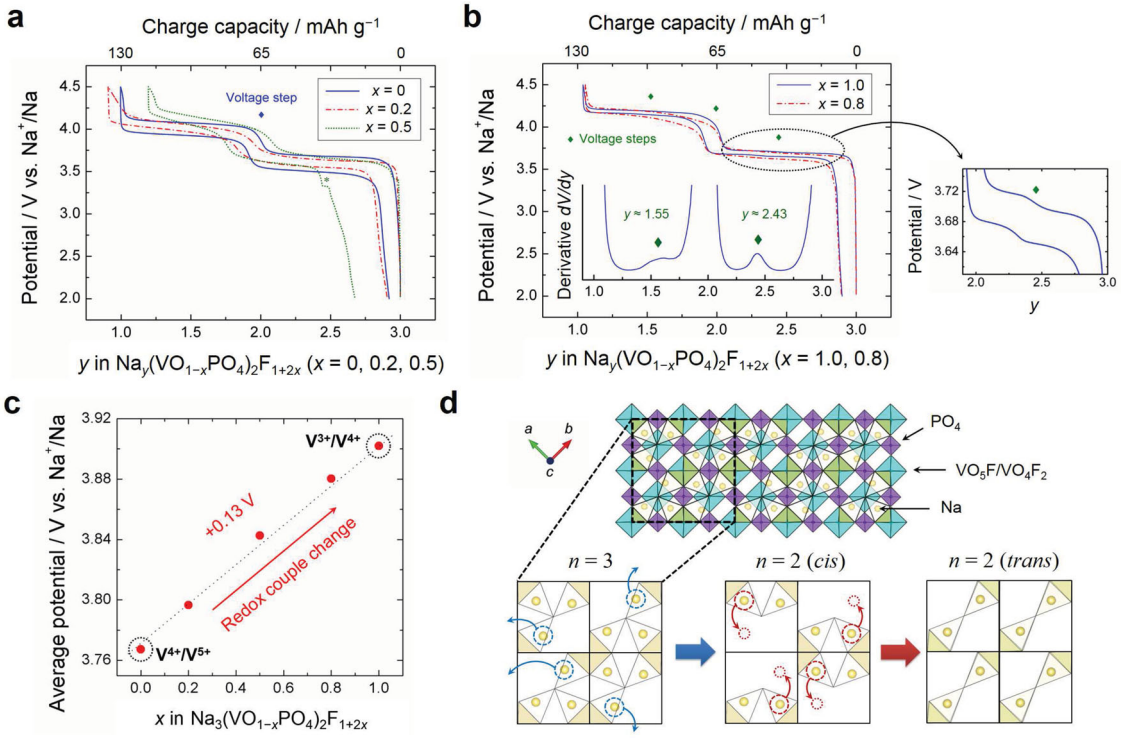

Figure 4. Voltage–composition curves of the $Na_y(VO_{1-x}PO_4)_2F_{1+2x}$ electrodes. (a) x = 0.0 (blue), 0.2 (red), and 0.5 (green). (b) x = 0.8 (red) and 1.0 (blue). The electrochemical cells were cycled at a *C*/10 rate with a voltage window of 2.0–4.5 V using the electrolyte of 1 M $NaBF_4$ in a mixture of EC and PC (1:1 v/v) at room temperature. Voltage steps are denoted by diamonds. A capacity region from $Na_3V_2(PO_4)_3$ for x = 0.5 is denoted by an asterisk. The inset and right panel of (b) show a derivative dV/dy analysis and enlarged voltage–composition curves for x = 1, respectively. (c) Change in average voltages of the $Na_y(VO_{1-x}PO_4)_2F_{1+2x}$ (x = 0.0, 0.2, 0.5, 0.8, and 1.0) electrodes. The redox couple was changed from V^{4+}/V^{5+} to V^{3+}/V^{4+} when x increased from 0 to 1, accompanied by a voltage increment of ~0.13 V. The average voltages were calculated on the basis of the areas under the voltage–composition curves in (a,b). (d) Evolution of Na-vacancy ordering in the $Na_y(VO_{1-x}PO_4)_2F_{1+2x}$ ($0 \le x \le 1$) electrodes as the pristine phase (y = 3.0) is transformed into the intermediate phase (y = 2.0). The Na extraction process (denoted by blue arrows) and Na-vacancy re-ordering process (denoted by red arrows) are schematically shown.

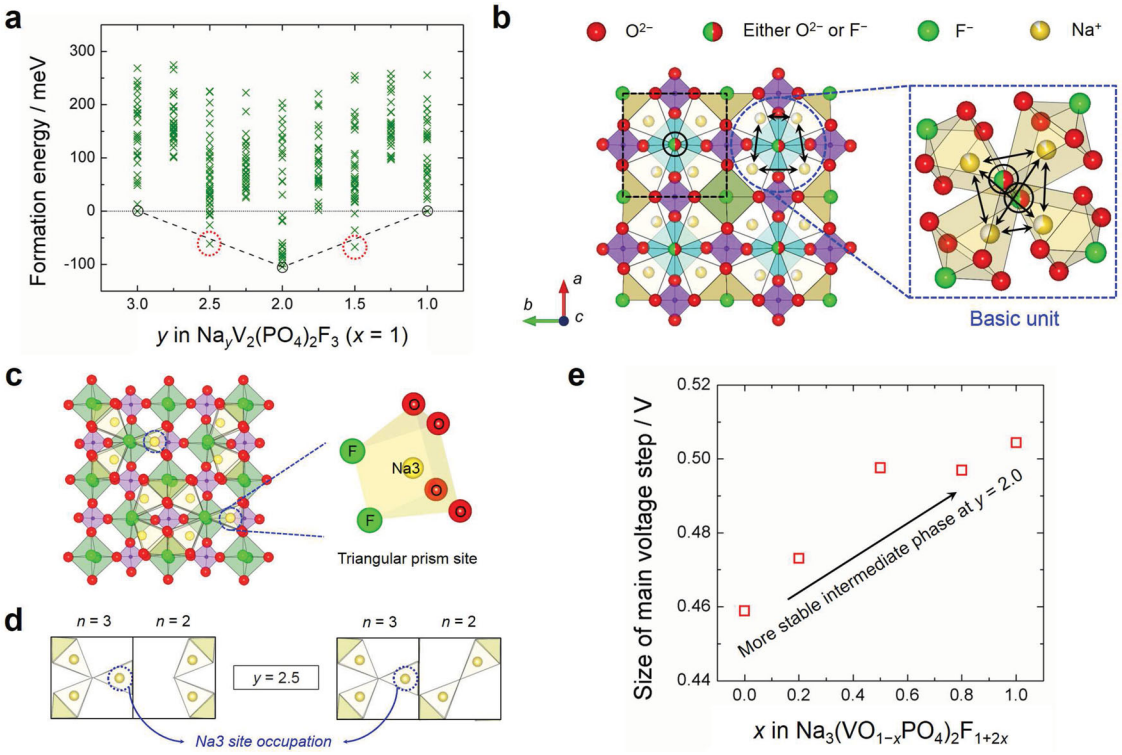

Figure 5. (a) Formation energy curve of $Na_yV_2(PO_4)_2F_3$ ($x = 1$) from first-principles calculations. (b) Intra-unit Na^+–Na^+ repulsion (denoted by arrows) in the Na layer of $Na_3(VO_{1-x}PO_4)_2F_{1+2x}$ ($0 \le x \le 1$). The unit refers to a basic unit (denoted by a dashed box). Anions that lie at the center of the basic unit (denoted by black circles) are purely O^{2-} and F^- for $x = 0$ and 1, respectively. For other x, both O^{2-} and F^- ions can be found in the site with a certain probability depending on x. The right panel shows a slightly tilted representation of the shielding of the Na^+–Na^+ repulsion by central O^{2-} or F^- ions in a basic unit. (c) Na-vacancy configuration on the Na layer of $Na_y(VO_{1-x}PO_4)_2F_{1+2x}$ ($x = 1$; $y = 2.5$) having Na3 sites (denoted by circles), obtained from first-principles calculations. The right panel shows the local environment for the Na3 site; one Na^+ ion is surrounded by four O^{2-} and two F^- ions, forming a triangular prism site. (d) Two possible unit–unit Na configurations including Na3 site occupation at $y = 2.5$. (e) Size variation of the main voltage step at $y \approx 2.0$ for the $Na_y(VO_{1-x}PO_4)_2F_{1+2x}$ ($0 \le x \le 1$) electrodes with increasing fluorine content (x). The sizes of the main voltage steps at $y \approx 2.0$ were calculated by subtracting the average voltages of the higher voltage region from those of the lower voltage region for the $Na_y(VO_{1-x}PO_4)_2F_{1+2x}$ ($x = 0.0$, 0.2, 0.5, 0.8, and 1.0) electrodes.

the intermediate phase.[26] A similar phenomenon has been observed for $x = 0.2$ in our previous work,[26] whose detailed discussion can be found in Supporting Information including Figure S6 and S7.

Another notable change in the electrochemical profile of $Na_y(VO_{1-x}PO_4)_2F_{1+2x}$ ($x = 0.8$ and 1.0) is the two additional voltage steps at $y \approx 2.43$ and 1.55 (Figure 4b), which appear as peaks in the corresponding derivative dV/dy curves (see the inset of Figure 4b and Supporting Information Figure S8). This suggests that additional intermediate phases were present at those compositions. First-principles calculations were carried out to determine the probability of different intermediate phases for different fluorine contents. **Figure 5**a shows a first-principles formation energy plot for $Na_yV_2(PO_4)_2F_3$ ($x = 1$) as a function of Na content. It was found that the stability at $y = 2.5$ and 1.5 was high compared to the formation energy plot of $Na_y(VOPO_4)_2F$ ($x = 0$) in our previous report.[26] The formation energies at $y = 2.5$ and 1.5 for $Na_yV_2(PO_4)_2F_3$ ($x = 1$) are both below the tie line at 0 K, implying the possibility of a stable intermediate phase at a finite temperature (denoted by circles in Figure 5a). In contrast, $Na_y(VOPO_4)_2F$ ($x = 0$) showed formation energies well above the tie line at the same compositions. The significantly lower formation energies of $Na_yV_2(PO_4)_2F_3$ ($x = 1$) compared to those of $Na_y(VOPO_4)_2F$ ($x = 0$) at these compositions imply a greater probability of voltage steps at $y \approx 2.5$ and 1.5 in the $Na_yV_2(PO_4)_2F_3$ ($x = 1$) electrode at room temperature. Some Na configurations for $Na_yV_2(PO_4)_2F_3$ ($x = 1$) and $Na_y(VOPO_4)_2F$ ($x = 0$) are provided in Supporting Information Figure S9 for both $y = 2.5$ and 1.5.

The relative stability of intermediate phases at certain Na and F compositions is likely attributable to the type and strength of the Na^+–Na^+ repulsion, which varied with the fluorine content in the $Na_y(VO_{1-x}PO_4)_2F_{1+2x}$ ($0 \le x \le 1$) electrodes. Figure 5b shows the main type of Na^+–Na^+ repulsion in the Na layer of $Na_3(VO_{1-x}PO_4)_2F_{1+2x}$ (denoted by arrows). The repulsion among Na^+ ions inside the basic unit is primarily shielded by anions that lie at the center of the basic unit (denoted by black circles), where the center anion can be O^{2-} or F^- depending on x. Previous work has shown that the substitution of F^- ions takes place at the center anion.[26,28] Because the shielding ability of less negative F^- ions is generally less effective than that of more negative O^{2-} ions, we believe that the intra-unit Na^+–Na^+ repulsion becomes stronger as x increases from 0 to 1. At $x = 0$, all the center positions are occupied by O^{2-} ions, and at $x = 1$, all are occupied by F^- ions. Thus, the stronger repulsion among Na^+ ions in $Na_yV_2(PO_4)_2F_3$ ($x = 1$) is believed to stabilize the

Na in a triangular prism site (denoted by circles in Figure 5c), which is the farthest from the other Na ions (see the first-principles calculations in Supporting Information Figure S9 for the stable Na configuration). Figure 5d shows a schematic representation of this new stable Na configuration within the basic unit, which minimizes the electrostatic repulsion among Na^+ ions. We also found that the voltage step at $y \approx 2.0$ for $Na_y(VO_{1-x}PO_4)_2F_{1+2x}$ ($0 \le x \le 1$) increased with increasing x, suggesting a more stable intermediate phase at $y \approx 2.0$ in fluorine-rich samples, as shown in Figure 5e. This is because samples with high x possess stronger intra-unit Na^+–Na^+ repulsion due to more intervening F^- ions with weaker shielding capability; therefore, the stable Na configuration that minimizes the Na^+–Na^+ repulsion becomes comparatively more important. However, exactly how the minimum formation energy at $y = 2.5$ and 1.5 could be below the tie lines for $x = 1.0$ is still unclear, because the different degree of shielding capability of O^{2-} and F^- ions is applied equally to all compositions of sodium (y). We believe that some particular Na-vacancy orderings (as shown in Figure 5d and Supporting Information Figure S9) somehow could be further stabilized at $x = 1.0$ as compared to $x = 0$, whose origin may be related to stronger inter-unit Na^+–Na^+ interactions at $x = 1.0$. The temperature-controlled experiment further confirmed that the appearance of the intermediate phases at certain Na contents arises due to the stabilization of Na-vacancy ordering. As the temperature increased, the thermal energy caused disorder of the Na and vacancies; thus, the Na-vacancy ordering became less visible. Electrochemical cycling performed at 60 °C showed that the dV/dy peaks at $y \approx 2.5$ became less prominent with increasing temperature (see Supporting Information, Figure S10), which originated from the disturbed Na-vacancy orderings due to thermal disordering.

The structural evolution of $Na_y(VOPO_4)_2F$ ($x = 0$) as a function of Na content (y) was investigated with ND and XRD, as shown in **Figure 6**a and b, respectively. While the change in the diffraction patterns with different Na contents was not significant due to the small change in the structure, a two-phase reaction was detected in the region of $2.0 \le y \le 3.0$ for both ND and XRD patterns. The high-angle region of the ND patterns in Figure 6a (denoted by a dotted box) show that the peak at ~111° emerged as the peak at ~109.5° disappeared, which is typical for a two-phase reaction. Furthermore, the peak splitting at ~28° and ~33° in the XRD patterns (denoted by dotted circles in Figure 6b) clearly indicates a biphasic nature. On the other hand, signs of a biphasic reaction in the region of $1.0 \le y \le 2.0$ were difficult to identify, despite the two-phase plateau in the electrochemical profile. This observation is similar to the previous report for $Na_y(VO_{0.8}PO_4)_2F_{1.4}$ ($x = 0.2$).[26] One possible reason for the difficulty in identifying the phases is that the difference of two phases in the region is not big with negligible change in the structure, and they are mixed at the atomic level with the coherent interface.[26] Figure 6c shows the change in lattice parameters upon desodiation of $Na_y(VOPO_4)_2F$ ($x = 0$). With decreasing Na content, lattice parameter a decreased linearly, whereas lattice parameter c increased linearly. During the desodiation process, the contraction of vanadium octahedra ($V^{4+} \rightarrow V^{5+}$) led to the decrease in lattice parameter a, whereas larger electrostatic repulsion between O^{2-} layers due to an emptier intervening Na layer caused the increase in lattice parameter c. Similar structural evolutions were observed for other compositions of x.[15,18,26,29] Supporting Information Figure S11 shows the evolution of XRD patterns in the region of $2.0 \le y \le 3.0$ for the $Na_yV_2(PO_4)_2F_3$ ($x = 1$) electrode. Behavior typical of a two-phase mixture is evident by a sudden broadening of the (220) peak. Nevertheless, we did not observe additional two-phase reactions near $y \approx 2.43$ and $y \approx 1.55$ by diffraction; these reactions were suggested from the electrochemical profile and the first-principles calculations. We are currently trying to identify these phases using other techniques. However, it should be noted that the interaction between different basic units, including long-range Na-vacancy ordering, was responsible for the stability of the phases at $y \approx 2.43$ and $y \approx 1.55$, and is relatively weak. Thus, the phase identification at ambient temperature may be more difficult.

The $Na_y(VOPO_4)_2F$ ($x = 0$) electrode exhibited a remarkably small volume change of –2.2% over the full charge range ($1.0 \le y \le 3.0$), as shown in Figure 6c. The volume changes were similar for $Na_y(VO_{1-x}PO_4)_2F_{1+2x}$ ($0 \le x \le 1$) with various fluorine contents, implying that the small volume change with Na de/insertion is characteristic of this family of compounds: –2.9% for $Na_y(VO_{0.8}PO_4)_2F_{1.4}$ ($x = 0.2$; $0.88 \le y \le 3.0$),[26] –1.79% for $Na_yV_2(PO_4)_2F_3$ ($x = 1$; $1.0 \le y \le 3.0$),[18] –2.12% for $Na_y(VO_{0.2}PO_4)_2F_{2.6}$ ($x = 0.8$; $1.0 \le y \le 3.0$), and –2.01% for $Na_y(VO_{0.5}PO_4)_2F_{2.0}$ ($x = 0.5$; $1.2 \le y \le 3.0$) (see Supporting Information Figure S12 for $x = 0.8$ and 0.5). The exceptionally small volume change gives rise to excellent cyclability for this family of cathode materials. Figure 6d and e show that the capacity retention and coulombic efficiencies of the $Na_3(VO_{1-x}PO_4)_2F_{1+2x}$ ($x = 0.0$, 0.2, 0.5, 0.8, and 1.0) electrodes were remarkably high. A substantial amount of the discharge capacity was well maintained for 150 cycles (90% for $x = 0.2$; 83% for $x = 0.5$; 81% for $x = 0.8$; 88% for $x = 1.0$) with high efficiency. The high voltage of ~4 V (vs. Na^+/Na) combined with the stable discharge capacity (>100 mAh g^{-1}) for all the electrodes in the family allows them to be categorized as a promising cathode group for NIBs. A relatively poor cycle stability was observed for $x = 0$, which agrees with the report by Sauvage et al.[15] The origin of this abnormal capacity fading for $x = 0$ is under investigation. The rate capability of this family of cathode materials is expected to be good as was previously reported for $Na_{1.5}VPO_5F_{0.5}$ framework (equivalent to $x = 0$) which allows facile Na diffusion along two types of two-dimensionally connected paths.[18,19,26–30]

2.3. Possibility of Multi-Electron Transfer in the $Na_y(VO_{1-x}PO_4)_2F_{1+2x}$ ($0 \le x \le 1$) System

A unique feature of $Na_y(VO_{1-x}PO_4)_2F_{1+2x}$ ($0 \le x \le 1$) is that its fluorine content can be tuned to utilize the multi-electron transfer of the vanadium redox reaction. **Figure 7** shows the voltage–composition curves of the $Na_y(VO_{1-x}PO_4)_2F_{1+2x}$ ($x = 0.0$, 0.5, and 1.0) electrodes from first-principles calculations. The $Na_y(VO_{1-x}PO_4)_2F_{1+2x}$ series exhibited a similar profile as two Na^+ ions were extracted from the structure, but showed distinct behavior during the third Na^+ ion extraction. Interestingly, the size of the voltage step at $y = 1.0$ was much larger than that at $y = 2.0$ for all x. This is attributable to two main factors: the

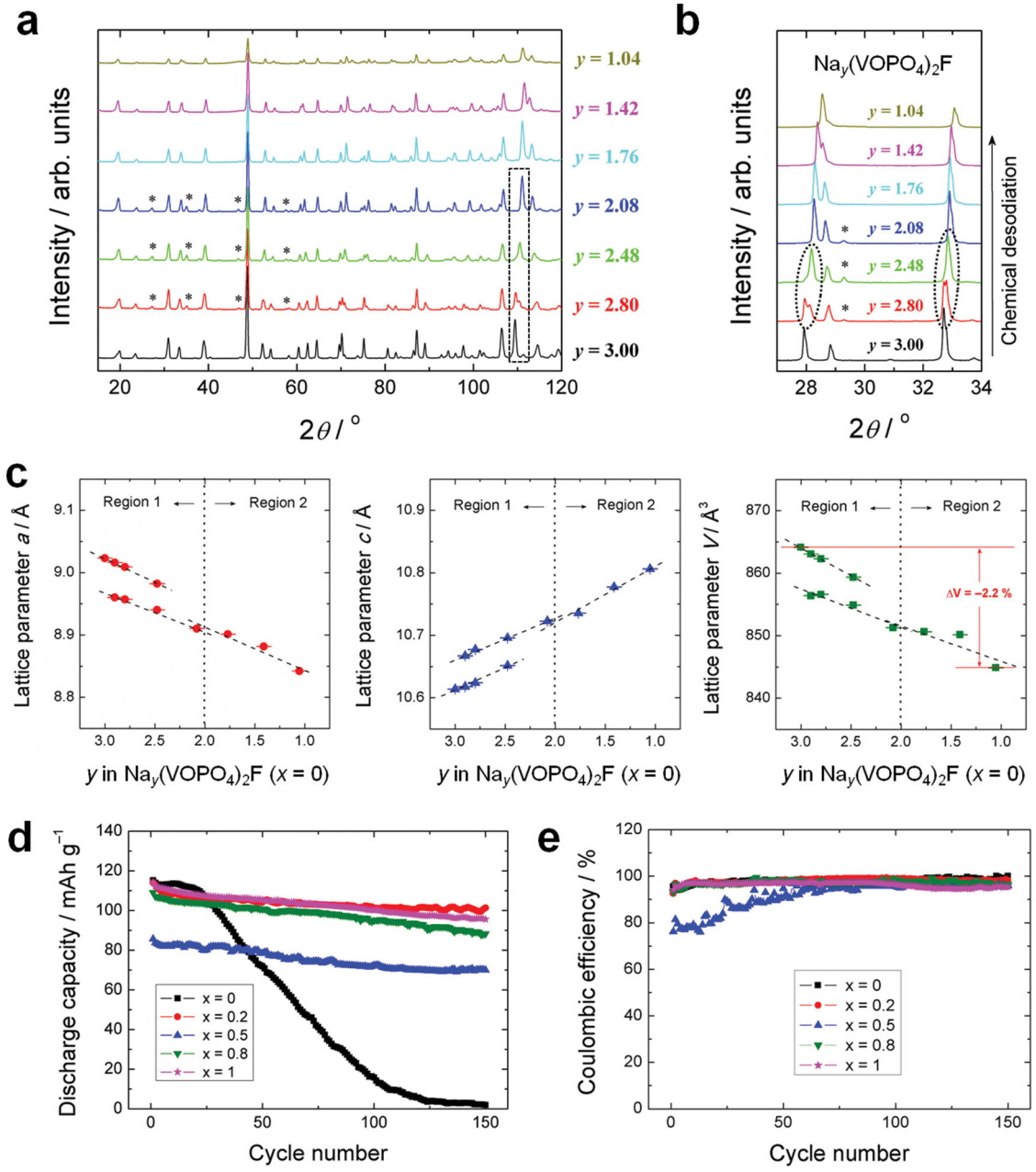

Figure 6. (a) ND and (b) XRD patterns of $Na_y(VOPO_4)_2F$ ($x = 0$; $1.0 \le y \le 3.0$) powders. Asterisks denote reflections of $NaNO_3$, which was produced during the chemical desodiation process in acetonitrile (CH_3CN) using NO_2BF_4 as the oxidant. (c) Lattice parameter changes with decreasing Na content (y) in $Na_y(VOPO_4)_2F$ ($x = 0$). Variation in (d) discharge capacity and (e) Coulombic efficiency of the $Na_3(VO_{1-x}PO_4)_2F_{1+2x}$ ($x = 0.0$, 0.2, 0.5, 0.8, and 1.0) electrodes for 150 cycles. The electrochemical cells were cycled at a $C/2$ rate with a voltage window of 2.0–4.5 V using the electrolyte of 1 M $NaPF_6$ in a mixture of EC and PC (1:1 v/v) at room temperature.

redox couple shift ($V^{3+}/V^{4+} \rightarrow V^{4+}/V^{5+}$ for $x = 1$; $V^{4+}/V^{5+} \rightarrow V^{5+}/V^{6+}$ for $x = 0$) and the presence of the stable intermediate phase at $y = 1.0$. For $x = 0$ (black line), it is noteworthy that the potential of the highest voltage plateau ($y \le 1.0$) related to the V^{5+}/V^{6+} redox couple is unusually high (i.e., far above 5 V vs. Na^+/Na), which is due to the fact that vanadium ions are hard to be oxidized to the V^{6+} state. For samples with $x = 0$ or $x = 1$, both of these factors clearly increased the potential during extraction of the third Na^+ ion. However, for samples with mixed V^{3+}/V^{4+} ions, an abrupt shift of the redox couple did not occur at $y = 1.0$. The mixed V^{3+} and V^{4+} ions continuously shifted the redox couple as y increased, as discussed before. This implies that the stability of the intermediate phase at $y = 1.0$ is solely responsible for the increased potential during the third Na^+ ion extraction in those cases. As a consequence, the predicted voltage for the third Na^+ ion extraction was notably lower at $x = 0.5$. Nevertheless, the potential for extracting the final, third Na^+ ion at $x = 0.5$ was greater than 4.5 V vs. Na^+/Na (denoted by a horizontal orange line in Figure 7), which is the onset potential for the decomposition of most Na electrolytes. Thus, reducing

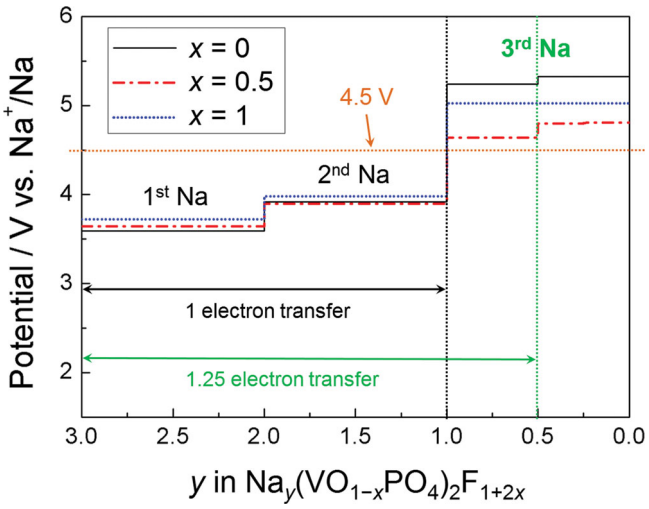

Figure 7. Voltage–composition curves for the $Na_y(VO_{1-x}PO_4)_2F_{1+2x}$ ($0 \leq x \leq 1$; $0 \leq y \leq 3$) electrodes from first-principles calculations: $x = 0$ (black), $x = 0.5$ (red), and $x = 1$ (blue). Vertical black and green lines denote one- and multi-electron transfer reactions, respectively. The horizontal orange line denotes 4.5 V (vs. Na^+/Na), above which the electrolyte starts to decompose.

the voltage step at $y = 1.0$ or making the step gentler so that some portion of the plateau remains below 4.5 V is expected to be important for utilizing the multi-electron transfer.

Interestingly, only the $Na_3(V^{3.8+}O_{0.8}PO_4)_2F_{1.4}$ ($x = 0.2$) sample showed the multi-electron transfer in the $Na_3(VO_{1-x}PO_4)_2F_{1+2x}$ ($0 \leq x \leq 1$) system (see Figure 4a), which we attribute to two factors. First, the sample with $x = 0.2$ exhibited weaker Na^+–Na^+ repulsion compared to the samples with $x = 0.8$ and 1.0. This is further evident by the much smaller voltage step at $y \approx 2.0$ (see Figure 5e). Therefore, the former is expected to have a much wider solid-solution region near the voltage steps, allowing additional Na^+ ions to be extracted below 4.5 V (vs. Na^+/Na). This implies that the samples with intermediate fluorine contents (such as $x = 0.2$, 0.5, and 0.8) are more beneficial for multi-electron transfer. Second, the slightly different redox potentials of the two redox couples, V^{3+}/V^{4+} and V^{4+}/V^{5+}, in mixed local environments can cause disorder in the operating voltage, which may make the voltage step at $y = 1.0$ gentler.

It is also possible to obtain a wider solid-solution region by substituting dopants in the Na layer to relieve the strong Na^+–Na^+ repulsion. In fact, in our previous report, the $Li_{1.1}Na_{0.4}VPO_{4.8}F_{0.7}$ ($x = 0.2$) electrode showed a negligible voltage step due to the much weaker Li^+–Li^+ repulsion, and thereby showed multi-electron transfer.[28] For NIB applications, the replacement of Na^+ ions by a small amount of other cations, such as H^+, Li^+, K^+, and Mg^{2+} ions, can be attempted. Furthermore, the substitution of other redox couples, such as Fe^{3+}, Ti^{3+}, and Cr^{3+} ions, may cause disorder and achieve multi-electron transfer.

3. Conclusion

We successfully synthesized a series of the isostructural $Na_3(VO_{1-x}PO_4)_2F_{1+2x}$ ($0 \leq x \leq 1$) compounds, in which the oxidation state of vanadium was altered by changing the fluorine content (x). The detailed electrochemical mechanisms of the $Na_y(VO_{1-x}PO_4)_2F_{1+2x}$ ($0 \leq x \leq 1$) electrodes were determined *via* a comparative study using a combined theoretical and experimental approach. The combination of different redox couples of V^{3+}/V^{4+} or V^{4+}/V^{5+}, Na^+–Na^+ ordering, and F/O distribution resulted in distinct voltage–composition curves and Na de/insertion mechanisms for the isostructural $Na_y(VO_{1-x}PO_4)_2F_{1+2x}$ family. We also found that all compositions in this system exhibited excellent electrochemical performance, attributable to the exceptionally small volume change upon cycling (~2%). The $Na_y(VO_{1-x}PO_4)_2F_{1+2x}$ electrodes have one of the highest energy densities (~520 Wh kg^{-1}) among NIB cathodes as well as ultrahigh stability, which allows them to be categorized as a promising cathode group. We believe that the thorough understanding of this system will pave the way for the design of high-performance electrode materials for NIBs.

4. Experimental Section

Sample Preparation: $Na_3(VO_{1-x}PO_4)_2F_{1+2x}$ (x = 0.0, 0.2, 0.5, 0.8, and 1.0) powders were prepared by a solid-state reaction using stoichiometric amounts of $VOPO_4$, VPO_4, NaF (Sigma-Aldrich, 99%), and Na_2CO_3 (Sigma-Aldrich, 99%) as precursors. Because the oxidation state of vanadium and the fluorine content simultaneously changed in this system due to the charge balance, we controlled the ratio of V^{3+} to V^{5+} precursors (i.e., VPO_4 and $VOPO_4$) rather than simply changing the amount of the fluorine precursor to prepare the $Na_3(VO_{1-x}PO_4)_2F_{1+2x}$ ($0 \leq x \leq 1$) compounds. The reaction is as follows:

$$(1-x)V^{5+}OPO_4 + xV^{3+}PO_4 + (1/2+x)NaF + [(1-x)/2]Na_2CO_3 \rightarrow 1/2Na_3(VO_{1-x}PO_4)_2F_{1+2x} + \text{gases}$$

Blending of the precursors was performed by high-energy ball-milling at 300 rpm for 24 h; the resulting mixtures were pelletized and sintered at 750 °C for 1.5 h under flowing argon. To prepare $VOPO_4$ powder, a stoichiometric amount of V_2O_5 (Sigma-Aldrich, 99%) and $NH_4H_2PO_4$ (Sigma-Aldrich, 99%) was mixed by high-energy ball-milling at 300 rpm for 24 h; the mixture was then pelletized and heat-treated at 750 °C for 4 h in air. To synthesize VPO_4 powder, a stoichiometric mixture of V_2O_5 and $NH_4H_2PO_4$, including 20 mol% Super P, was mixed by high-energy ball-milling, also at 300 rpm for 24 h; the mixture was then pelletized and heat-treated at 850 °C for 2 h under an Ar atmosphere. To obtain $Na_y(VOPO_4)_2F$ ($x = 0$) powders with various Na contents ($1.0 \leq y \leq 3.0$), the $Na_3(VOPO_4)_2F$ ($x = 0$) powders were chemically oxidized using a stoichiometric amount of NO_2BF_4 (Sigma-Aldrich, 95%) in the solvent of acetonitrile (Sigma-Aldrich, 99.8%) at room temperature. After reacting for 16 h, the powders were washed, centrifuged several times with acetonitrile and ethanol, and then dried in a vacuum oven at 70 °C.

Elemental Analysis and Morphology: The atomic ratios of sodium, vanadium, and phosphorus in the series of samples were determined by inductively coupled plasma (ICP) spectroscopy (Polyscan 60E; Thermo Jarrell Ash, USA). Scanning electron microscopy (SEM) images were obtained using a SUPRA 55VP FE-SEM (Carl Zeiss, Germany) at an operating voltage of 2 kV. Fluorine contents in the $Na_3(VO_{1-x}PO_4)_2F_{1+2x}$ ($0 \leq x \leq 1$) samples were further verified using energy-dispersive X-ray spectroscopy (EDS) (X-Flash spectrometer; Bruker, Germany) at an operating voltage of 15 kV. Transmission electron microscopy (TEM) images were acquired using a Tecnai F20 (FEI, USA) and JEM-3000F/JEM-2100F (JEOL, Japan) at an accelerating voltage of 200 kV.

Global and Local Structure of $Na_3(VO_{1-x}PO_4)_2F_{1+2x}$: Neutron diffraction (ND) data were collected over the 2θ range of 0–180° with a step size of 0.05°, and a wavelength of $\lambda = 1.83429$ Å was supplied by a Ge(331) single-crystal monochromator on a high-resolution powder diffractometer (HRPD) at the Hanaro facility of the Korea

Atomic Energy Research Institute. X-ray diffraction (XRD) spectra were obtained using an X-ray diffractometer (D8 Advance; Bruker, Germany) with Ni-filtered Cu Kα radiation (λ = 1.5406 Å) over the 2θ range of 10–60°. High-resolution XRD using synchrotron radiation was carried out at beam line 9B at the Pohang Accelerator Laboratory (PAL) with an average wavelength of 1.5475 Å. The room-temperature ND/XRD data were refined using the Rietveld method and Fullprof software.[46] The crystal structures were drawn using the VESTA program.[47] X-ray absorption near-edge structure (XANES) spectra were recorded at room temperature at beam line 7D at the PAL using photons with a storage ring energy of 2.5 GeV and a current range of 100–140 mA. The spectra were collected in the transmission mode at the vanadium K-edge. Solid-state ^{23}Na magic-angle spinning (MAS) nuclear magnetic resonance (NMR) spectroscopy experiments were performed using a Bruker Avance 400 MHz 9.4 T wide-bore spectrometer (4 mm probe) at a Larmor frequency of 105.8 MHz. The shifts were referenced to 0.1 M NaCl (0 ppm). All spectra were obtained using a 90° pulse of 1 μs and a recycle time of 0.5 s with a MAS frequency of either 15 or 17 kHz at room temperature.

Electrochemical Characterization: Slurries of 70 wt% $Na_3(VO_{1-x}PO_4)_2F_{1+2x}$ (x = 0.0, 0.2, 0.5, 0.8, and 1.0) powders, 20 wt% carbon black, and 10 wt% polyvinylidene fluoride (PVDF, Sigma-Aldrich) dispersed in *N*-methyl-2-pyrrolidone (NMP, Sigma-Aldrich) were prepared, cast on Al foil, and dried at 120°C for the electrode fabrication. The loadings of the active material on the electrodes were ~3 mg cm^{-2}. Electrochemical cells were assembled into CR2032-type coin cells in an Ar-filled glove box (MBraun, Germany). Na metal (Sigma-Aldrich) and a glass microfiber filter (grade GF/F; Whatman, USA) were used as a counter electrode and separator, respectively. All electrochemical tests were performed using a potentiostat/galvanostat (WBCS 3000; WonA Tech, Korea) with an electrolyte of 1 M $NaBF_4$ or $NaPF_6$ in a mixture of ethyl carbonate (EC) and propylene carbonate (PC) (1:1 v/v). To prepare the $Na_y(VO_{1-x}PO_4)_2F_{1+2x}$ (x = 0.0, 0.2, 0.5, 0.8, and 1.0) electrodes for *ex-situ* experiments, the electrochemical cells were galvanostatically charged or discharged at a *C*/10 rate and disassembled at various states of charge (SOC). Prior to the *ex-situ* experiments, the electrodes were washed with PC and dried overnight in vacuum at 70°C. Based on one-electron transfer, 1*C* rates were calculated to correspond to ~130 mA g^{-1} for the $Na_y(VO_{1-x}PO_4)_2F_{1+2x}$ (x = 0.0, 0.2, 0.5, 0.8, and 1.0) electrodes.

Computational Methods: First-principles calculations were carried out using the Perdew–Burke–Ernzerhof exchange-correlation parameterization to density functional theory (DFT) with the spin-polarized generalized gradient approximation (GGA).[48] We used a plane-wave basis set and the projector-augmented wave (PAW) method, as implemented in the Vienna ab initio simulation package (VASP).[49] Hubbard parameters (GGA+*U*)[50] were added to correct the incomplete cancellation of the self-interaction of GGA. We calculated redox potentials of V^{4+}/V^{5+} in $Na_y(VOPO_4)_2F$ (x = 0) and V^{3+}/V^{4+} in $Na_yV_2(PO_4)_2F_3$ (x = 1) with various *U* values (see Supporting Information Figure S13). The calculated redox potentials for both compounds were in the best agreement with the experimental values when *U* value was 4.0 eV, thus we used this *U* value for vanadium ions of the family of $Na_y(VO_{1-x}PO_4)_2F_{1+2x}$ ($0 \le x \le 1$). To study the $Na_y(VO_{1-x}PO_4)_2F_{1+2x}$ (x = 0.0, 0.5, and 1.0) electrodes, we considered all possible Na-vacancy orderings within the unit cell of $Na_y(VO_{1-x}PO_4)_2F_{1+2x}$ ($0 \le y \le 3$) generated with the CASM program.[51] From the results, we selected thirty Na-vacancy orderings with the lowest electrostatic energy at each composition through the Ewald summation method[52] and then calculated their energies with GGA+*U*. We used a plane wave basis set with sampling the Monkhorst-Pack 4 × 4 × 4 *k*-point mesh. The double-sized supercells containing 8 formula units were additionally explored to determine the energies of the intermediate phases at y = 2.5 and 1.5 because long-range Na^+–Na^+ interactions in the larger supercell may further stabilize the structure. We determined voltage profiles of the $Na_y(VO_{1-x}PO_4)_2F_{1+2x}$ ($0 \le y \le 3$; x = 0.0, 0.5, and 1.0) electrodes using the following equation:

$$\langle V \rangle = -[E(Na_{y1}(VO_{1-x}PO_4)_2F_{1+2x}) - E(Na_{y2}(VO_{1-x}PO_4)_2F_{1+2x}) - (y_1 - y_2) \times E(Na)] \div [(y_1 - y_2) \times F]$$

where E is the DFT energy of the structure and F is the Faraday constant.

Supporting Information

Supporting Information is available from the Wiley Online Library or from the author.

Acknowledgements

This work was supported by the Human Resources Development program (20124010203320) of the Korea Institute of Energy Technology Evaluation and Planning (KETEP) grant and the World Premier Materials grant funded by the Korea government Ministry of Trade, Industry and Energy. This work was also supported by the Supercomputing Center/Korea Institute of Science and Technology Information with supercomputing resources including technical support (KSC-2012-C2-78), the Research Center Program of IBS (Institute for Basic Science) in Korea, and NRF (National Research Foundation of Korea) Grant funded by the Korean Government (NRF-2011-Global Ph.D. Fellowship Program)

Received: February 18, 2014
Revised: March 3, 2014
Published online: April 22, 2014

[1] S.-W. Kim, D.-H. Seo, X. Ma, G. Ceder, K. Kang, *Adv. Energy Mater.* **2012**, *2*, 710.
[2] V. Palomares, P. Serras, I. Villaluenga, K. B. Hueso, J. Carretero-Gonzalez, T. Rojo, *Energy Environ. Sci.* **2012**, *5*, 5884.
[3] H. Pan, Y.-S. Hu, L. Chen, *Energy Environ. Sci.* **2013**, *6*, 2338.
[4] B. L. Ellis, L. F. Nazar, *Curr. Opin. Solid State Mater. Sci.* **2012**, *16*, 168.
[5] M. D. Slater, D. Kim, E. Lee, C. S. Johnson, *Adv. Funct. Mater.* **2013**, *23*, 947.
[6] V. Palomares, M. Casas-Cabanas, E. Castillo-Martinez, M. H. Han, T. Rojo, *Energy Environ. Sci.* **2013**, *6*, 2312.
[7] S. Y. Hong, Y. Kim, Y. Park, A. Choi, N.-S. Choi, K. T. Lee, *Energy Environ. Sci.* **2013**, *6*, 2067.
[8] Y. Wang, X. Yu, S. Xu, J. Bai, R. Xiao, Y.-S. Hu, H. Li, X.-Q. Yang, L. Chen, X. Huang, *Nat. Commun.* **2013**, *4*, 2365.
[9] N. Yabuuchi, M. Kajiyama, J. Iwatate, H. Nishikawa, S. Hitomi, R. Okuyama, R. Usui, Y. Yamada, S. Komaba, *Nat. Mater.* **2012**, *11*, 512.
[10] M. Guignard, C. Didier, J. Darriet, P. Bordet, E. Elkaïm, C. Delmas, *Nat. Mater.* **2013**, *12*, 74.
[11] N. Yabuuchi, M. Yano, H. Yoshida, S. Kuze, S. Komaba, *J. Electrochem. Soc.* **2013**, *160*, A3131.
[12] P. Vassilaras, X. Ma, X. Li, G. Ceder, *J. Electrochem. Soc.* **2013**, *160*, A207.
[13] R. Berthelot, D. Carlier, C. Delmas, *Nat. Mater.* **2011**, *10*, 74.
[14] Z. Jian, W. Han, X. Lu, H. Yang, Y.-S. Hu, J. Zhou, Z. Zhou, J. Li, W. Chen, D. Chen, L. Chen, *Adv. Energy Mater.* **2013**, *3*, 156.
[15] F. Sauvage, E. Quarez, J. M. Tarascon, E. Baudrin, *Solid State Sciences* **2006**, *8*, 1215.

[16] H. Zhuo, X. Wang, A. Tang, Z. Liu, S. Gamboa, P. J. Sebastian, *J. Power Sources* **2006**, *160*, 698.
[17] Z.-m. Liu, X.-y. Wang, Y. Wang, A.-p. Tang, S.-y. Yang, L.-f. He, *Trans. Nonferrous Metals Soc. China* **2008**, *18*, 346.
[18] R. A. Shakoor, D.-H. Seo, H. Kim, Y.-U. Park, J. Kim, S.-W. Kim, H. Gwon, S. Lee, K. Kang, *J. Mater. Chem.* **2012**, *22*, 20535.
[19] K. Chihara, A. Kitajou, I. D. Gocheva, S. Okada, J.-i. Yamaki, *J. Power Sources* **2013**, *227*, 80.
[20] M. Xu, L. Wang, X. Zhao, J. Song, H. Xie, Y. Lu, J. B. Goodenough, *Phys. Chem. Chem. Phys.* **2013**, *15*, 13032.
[21] P. Moreau, D. Guyomard, J. Gaubicher, F. Boucher, *Chem. Mater.* **2010**, *22*, 4126.
[22] H. Kim, R. A. Shakoor, C. Park, S. Y. Lim, J.-S. Kim, Y. N. Jo, W. Cho, K. Miyasaka, R. Kahraman, Y. Jung, J. W. Choi, *Adv. Funct. Mater.* **2013**, *23*, 1147.
[23] P. Barpanda, T. Ye, S.-i. Nishimura, S.-C. Chung, Y. Yamada, M. Okubo, H. Zhou, A. Yamada, *Electrochem. Commun.* **2012**, *24*, 116.
[24] Y. Kawabe, N. Yabuuchi, M. Kajiyama, N. Fukuhara, T. Inamasu, R. Okuyama, I. Nakai, S. Komaba, *Electrochem. Commun.* **2011**, *13*, 1225.
[25] H. Kim, I. Park, D.-H. Seo, S. Lee, S.-W. Kim, W. J. Kwon, Y.-U. Park, C. S. Kim, S. Jeon, K. Kang, *J. Am. Chem. Soc.* **2012**, *134*, 10369.
[26] Y.-U. Park, D. H. Seo, H.-S. Kwon, B. Kim, J. Kim, H. Kim, I. Kim, H.-I. Yoo, K. Kang, *J. Am. Chem. Soc.* **2013**, *135*, 13870.
[27] P. Serras, V. Palomares, A. Goni, I. Gil de Muro, P. Kubiak, L. Lezama, T. Rojo, *J. Mater. Chem.* **2012**, *22*, 22301.
[28] Y.-U. Park, D.-H. Seo, B. Kim, K.-P. Hong, H. Kim, S. Lee, R. A. Shakoor, K. Miyasaka, J.-M. Tarascon, K. Kang, *Sci. Rep.* **2012**, *2*, 704.
[29] P. Serras, V. Palomares, J. Alonso, N. Sharma, J. M. López del Amo, P. Kubiak, M. L. Fdez-Gubieda, T. Rojo, *Chem. Mater.* **2013**, *25*, 4917.
[30] P. Serras, V. Palomares, A. Goñi, P. Kubiak, T. Rojo, *J. Power Sources* **2013**, *241*, 56.
[31] A. A. Tsirlin, R. Nath, A. M. Abakumov, Y. Furukawa, D. C. Johnston, M. Hemmida, H. A. Krug von Nidda, A. Loidl, C. Geibel, H. Rosner, *Phys. Rev. B* **2011**, *84*, 014429.
[32] W. Massa, O. V. Yakubovich, O. V. Dimitrova, *Solid State Sciences* **2002**, *4*, 495.
[33] J. Barker, M. Y. Saidi, J. L. Swoyer, *Electrochem. Solid-State Lett.* **2003**, *6*, A1.
[34] J. M. Le Meins, M. P. Crosnier-Lopez, A. Hemon-Ribaud, G. Courbion, *J. Solid State Chem.* **1999**, *148*, 260.
[35] J. Barker, R. K. B. Gover, P. Burns, A. J. Bryan, *Electrochem. Solid-State Lett.* **2006**, *9*, A190.
[36] R. K. B. Gover, A. Bryan, P. Burns, J. Barker, *Solid State Ionics* **2006**, *177*, 1495.
[37] T. Jiang, G. Chen, A. Li, C. Wang, Y. Wei, *J. Alloys Compd.* **2009**, *478*, 604.
[38] P. Y. Zavalij, M. S. Whittingham, *Acta Crystallogr. B* **1999**, *55*, 627.
[39] W. Baur, *Acta Crystallogr. B* **1974**, *30*, 1195.
[40] J. Yoon, S. Muhammad, D. Jang, N. Sivakumar, J. Kim, W.-H. Jang, Y.-S. Lee, Y.-U. Park, K. Kang, W.-S. Yoon, *J. Alloys Compd.* **2013**, *569*, 76.
[41] J. Wong, F. W. Lytle, R. P. Messmer, D. H. Maylotte, *Phys. Rev. B* **1984**, *30*, 5596.
[42] C. P. Grey, N. Dupré, *Chem. Rev.* **2004**, *104*, 4493.
[43] D. Carlier, M. Menetrier, C. P. Grey, C. Delmas, G. Ceder, *Phys. Rev. B* **2003**, *67*, 174103.
[44] B. L. Ellis, T. N. Ramesh, L. J. M. Davis, G. R. Goward, L. F. Nazar, *Chem. Mater.* **2011**, *23*, 5138.
[45] A. J. Bard, L. R. Faulkner, *Electrochemical Methods: Fundamentals and Applications*, Vol. 2, Wiley, New York **1980**.
[46] T. Roisnel, J. Rodríguez-Carvajal, *Mater. Sci. Forum* **2001**, *378–381*, 118.
[47] K. Momma, F. Izumi, *J. Appl. Crystallogr.* **2008**, *41*, 653.
[48] J. P. Perdew, K. Burke, M. Ernzerhof, *Phys. Rev. Lett.* **1996**, *77*, 3865.
[49] G. Kresse, J. Furthmüller, *Comp. Mater. Sci.* **1996**, *6*, 15.
[50] V. I. Anisimov, J. Zaanen, O. K. Andersen, *Phys. Rev. B* **1991**, *44*, 943.
[51] A. Van der Ven, J. C. Thomas, Q. Xu, B. Swoboda, D. Morgan, *Phys. Rev. B* **2008**, *78*, 104306.
[52] A. Y. Toukmaji, J. A. Board Jr, *Comput. Phys. Commun.* **1996**, *95*, 73.